

# High-Fidelity Text-to-Image Generation from Pre-Trained Vision-Language Models via Distribution-Conditioned Diffusion Decoding

Ji Woo Hong<sup>1</sup> Hee Suk Yoon<sup>1</sup> Gwanhyeong Koo<sup>1</sup> Eunseop Yoon<sup>1</sup> SooHwan Eom<sup>1</sup> Qi Dai<sup>2</sup> Chong Luo<sup>2</sup>  
Chang D. Yoo<sup>1</sup>

## Abstract

Recent large-scale vision–language models (VLMs) have shown remarkable text-to-image generation capabilities, yet their visual fidelity remains constrained by the discrete image tokenization, which poses a major challenge. Although several studies have explored continuous representation modeling to enhance visual quality, adapting pre-trained VLM models to such representations requires large-scale data and training costs comparable to the original pre-training. To circumvent this limitation, we propose a diffusion-based decoding framework that enhances image fidelity by training only a diffusion decoder on the output image-token logits of pre-trained VLMs, thereby preserving the original model intact. At its core, Logit-to-Code Distributional Mapping converts the VLM’s image-token logits into continuous, distribution-weighted code vectors with uncertainty features, providing an effective conditioning signal for diffusion decoding. A lightweight Logit Calibration aligns training-time proxy logits from the VQ-VAE encoder with VLM-generated logits, mitigating the train–inference gap. Conditioned on these representations, the Distribution-Conditioned Diffusion Decoder generates high-fidelity images. Achieved solely through short training on ImageNet-1K, our method consistently improves visual fidelity for both VQ-VAE reconstructions and text-to-image generations from VLM-predicted tokens.

<sup>1</sup>Korea Advanced Institute of Science and Technology (KAIST), Daejeon, Republic of Korea <sup>2</sup>Microsoft Research Asia (MSRA), Beijing, China. Correspondence to: Chong Luo <chong.luo@microsoft.com>, Chang D. Yoo <cd.yoo@kaist.ac.kr>.

This work was done while Ji Woo Hong was an intern at MSRA.



Figure 1. Comparison of visual reconstruction quality from VQ-VAE–encoded representations. While the VQ-VAE decoded output exhibits shape distortion and loss of detail, our diffusion-based method consistently improves image fidelity, preserving structural accuracy and fine-grained visual sharpness.

## 1. Introduction

Recent publicly available vision-language models (VLMs) (Chen et al., 2025; Sun et al., 2024) have demonstrated remarkable performance in Autoregressive (AR) image generation. Despite these advancements, their visual fidelity remains fundamentally limited by the use of discrete image tokenization (Van Den Oord et al., 2017; Esser et al., 2021). The images reconstructed from discrete tokens often contains distorted or imprecise shapes, as shown in Figure 1, underscoring the gap between the VLM’s strong semantic capabilities and its limited visual precision.

As VLMs grow in semantic capability, this limitation has become the primary obstacle to high-fidelity synthesis. Performance is increasingly capped not by the VLM itself, but by the decoder’s discretization. Addressing this bottleneck is therefore essential for reliable, high-quality generation. Recent works have attempted two main approaches to mitigate this issue. The first replaces discrete tokenizers with continuous or hybrid representations, aiming to improve token’s expressiveness (Wang et al., 2025; Wu et al., 2025; Tang et al., 2024; Li et al., 2024b). The second combines pre-trained VLMs with diffusion-based decoder that refine

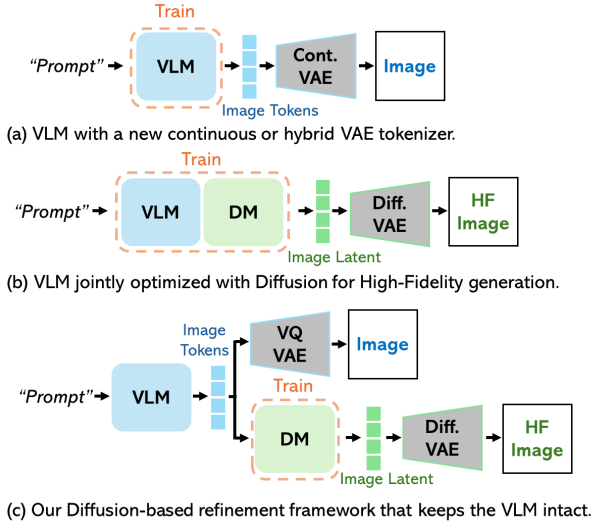


Figure 2. Conceptual comparison of different strategies for improving visual fidelity in VLM image generation. (a) Tokenizer replacement re-trains the entire VLM with a new continuous or hybrid tokenizer. (b) Diffusion-assisted decoding jointly optimizes the VLM and diffusion model, altering the original VLM. (c) Ours train only the diffusion-based decoder, preserving VLM’s original capabilities.

or regenerate outputs with improved quality (Geng et al., 2025; Xie et al., 2024; Huang et al., 2025). While these two prior directions have made their contributions, they both entail substantial training overhead. Tokenizer replacement requires re-training the VLM from scratch to accommodate a new token format, essentially demanding a training of a new foundation model. Furthermore, joint optimization of the VLM and diffusion model makes the VLM inherently dependent on diffusion-based generation, forfeiting the lightweight VQ-VAE decoding pathway. These two directions are conceptually illustrated in Figure 2. In Figure 2 (a), the adoption of a new tokenizer requires re-training of the VLM, and approach Figure 2 (b) augments the VLM with diffusion decoding which involves joint training to align the two models.

We propose a novel framework for improving image fidelity from pre-trained VLMs without modifying their parameters, by reinterpreting and exploiting their internal token-generation process. Unlike prior diffusion-assisted approaches that jointly optimize the VLM and the diffusion model, our framework keeps the VLM entirely intact and trains only a diffusion-based decoder, as illustrated in Figure 2(c). This design is motivated by a key observation that, although VLMs ultimately outputs discrete image tokens, their generation process inherently involves rich internal continuous representations prior to discretization. These image-token logits encode the model’s confidence over multiple visual codebook entries, capturing fine-grained appearance cues and local ambiguities that are discarded by hard token selection. Despite being readily available during infer-

ence, such logit distributions have not been systematically exploited as conditioning signals for downstream image synthesis. Building on this observation, we introduce a framework that elevates VLM image-token logit distributions to rich conditioning representations for diffusion-based decoding. This is achieved through three tightly coupled components, summarized in Figure 3.

**Logit-to-Code Distributional Mapping (LCDM):** LCDM is a framework that converts the VLM’s *Image-Token Logits* distribution into continuous conditioning representations for the diffusion decoder. Given the logit vector at each spatial token, LCDM derives a probability distribution over the visual *Codebook*, explicitly preserving the relative confidence structure encoded by the VLM. These distributions are then projected into the codebook embedding space to form *Distribution-Weighted Code Vectors*, which serve as continuous semantic embeddings for each image patch. While the aggregation operation itself resembles an expectation over codebook entries, its role here is not merely to smooth discrete tokens, but to retain and expose the latent uncertainty inherent in the VLM’s predictions, which is otherwise lost under hard token selection. In parallel, LCDM extracts complementary *Uncertainty Features* that quantify prediction confidence and ambiguity, providing the diffusion model with uncertainty-aware conditioning signals. Together, these representations transform raw VLM logits into a diffusion conditioning space that preserves both semantic content and predictive uncertainty.

**Logit Calibration (LC):** A major challenge in training diffusion decoders from VLM-derived representations is the absence of ground-truth logit distributions during training. To address this, we approximate inference-time VLM logits using *Proxy Image-Token Logits* obtained from the VQ-VAE encoder employed in the VLM’s tokenization pipeline. However, these proxy logits exhibit markedly different confidence and entropy characteristics compared to the VLM’s true predictions, resulting in a significant train–inference mismatch. Logit Calibration resolves this discrepancy by explicitly aligning the distributional statistics of proxy logits with those of the VLM. We extract *Target Distribution Statistics* from the VLM’s image-token logits, and calibrate the proxy logits via lightweight affine scaling, temperature adjustment, and label smoothing. This process ensures that diffusion training is conducted under conditioning distributions that faithfully reflect the VLM’s intrinsic uncertainty structure, making the proposed framework viable without direct access to the VLM during training.

**Distribution-Conditioned Diffusion Decoder (DCDD):** Conditioned on the calibrated, distribution-aware representations produced by LCDM and LC, we employ a diffusion model as a high-fidelity decoder. Rather than training from scratch, we leverage an inpainting diffusion transformer,

FLUX.1-Fill (Labs et al., 2025), which is well-suited for localized refinement guided by token-level conditions.

By only training the diffusion components, our method surpass the performance of the VQ-VAE decoder through short training on the ImageNet-1K (Russakovsky et al., 2015).

## 2. Related Works

### Continuous and Hybrid Tokenization for AR Models:

One line of approaches seeks to improve image fidelity by training new autoregressive (AR) models from scratch using improved image tokenization schemes. Representative works explore continuous tokenization or hybrid representations that combine discrete structure tokens with continuous latent features to reduce quantization artifacts and better preserve fine-grained details. TokenBridge (Wang et al., 2025) and Li et al. (Li et al., 2024b) belong to this category by either decoupling quantization from training or fully replacing discrete codebooks with continuous latent spaces. Another group of methods adopts hybrid tokenization strategies, where discrete tokens capture global structure while continuous residuals model fine details, as explored in HART (Tang et al., 2024) and DC-AR (Wu et al., 2025).

**AR Models with Diffusion-Based Decoding:** Another line of research integrates diffusion models into autoregressive pipelines to boost image quality by combining semantic reasoning with pixel-level refinement. Some methods improve AR generation by aligning it with diffusion-based decoders through additional optimization objectives, such as reinforcement learning, as in X-Omni (Geng et al., 2025). Other approaches incorporate diffusion more tightly into multimodal generation pipelines: UniFusion (Li et al., 2025) leverages a vision-language model (VLM) as a unified encoder to condition diffusion-based image generation, while Show-o (Xie et al., 2024) and ILLUME+ (Huang et al., 2025) further unify multimodal understanding and image generation through architectures that combine autoregressive modeling with diffusion-based decoding.

Despite their strong performance, these approaches share limitations that make them unsuitable for our problem. Methods based on continuous or hybrid tokenization require retraining AR models together with custom tokenizers on large-scale datasets comparable to those used for building new foundation models. Meanwhile, diffusion-based decoding approaches either train new multimodal foundation models from scratch or tightly couple pre-trained language models with diffusion during training, making diffusion an integral component of image generation and necessitating additional optimization to preserve multimodal understanding capabilities. In contrast, our goal is to enhance the visual fidelity of images directly generated by an existing

pre-trained VLM without modifying it. To this end, we keep the VLM frozen and treat diffusion as an optional decoding module that reconstructs the VLM outputs into high-fidelity images. This design preserves the original semantics and intent of the VLM, minimizing diffusion-induced semantic drift, and allows reverting to standard VQ-VAE decoding when computational efficiency is preferred.

## 3. Conceptual Motivation

**Autoregressive Image Token Generation:** Autoregressive vision-language models generate images by predicting sequences of discrete image tokens conditioned on a text prompt. At each generation step  $i$ , the transformer decoder produces a hidden representation that is projected into a vector of image-token logits  $\mathbf{l}_i \in \mathbb{R}^K$ , where each dimension corresponds to an entry in a VQ-VAE codebook. The next image token is selected according to these logits, and the full token sequence is subsequently decoded into pixel space by a VQ-VAE decoder.

Although the final output consists of discrete token indices, the generation process itself is governed by continuous neural representations. In particular, the image-token logits encode a continuous belief over the codebook entries, reflecting how strongly the model’s internal state aligns with each visual prototype. Viewing these logits as a probability distribution over code vectors reveals a continuous representation that preserves the semantic structure of the VLM’s internal space. This perspective provides a conceptual bridge between the discrete token space of autoregressive VLMs and continuous latent spaces for diffusion-based decoding.

**VQ-VAE Encoding for Token Supervision:** During training, images are mapped to discrete supervision targets using a VQ-VAE encoder. The encoder downsamples an image into a grid of latent image-token features  $\mathbf{f}_{i,j} \in \mathbb{R}^D$ , each of which is quantized to its nearest codebook entry,  $x_{i,j} = \arg \min_k \|\mathbf{f}_{i,j} - \mathbf{e}_k\|_2^2$ . These discrete indices are used as supervision for autoregressive token prediction.

While supervision is discrete, the quantization process itself is driven by continuous feature-to-code similarity. This structure mirrors the mechanism by which a VLM produces image-token logits, which measure the alignment between its hidden representations and the same codebook entries. As a result, both the VQ-VAE encoder and the VLM implicitly encode continuous similarity relationships over the codebook, albeit with different confidence characteristics and distributional properties.

**Calibration between VLM and VQ-VAE:** Despite their shared alignment structure, the probability distributions produced by the VQ-VAE encoder and the VLM differ substantially in sharpness and entropy. The VLM typically assigns high probability mass to a small number of semanti-

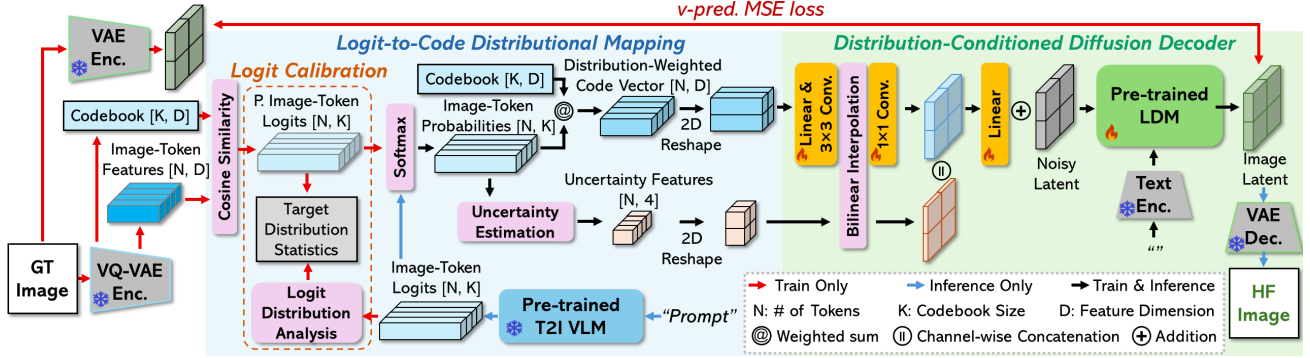


**Figure 3. Overview of our proposed framework.** During inference, the pre-trained VLM produces Image-Token Logits, which are transformed in the Logit-to-Code Distributional Mapping stage into continuous Distribution-Weighted Code Vectors and complementary Uncertainty Features capturing the reliability and ambiguity of each token prediction. These continuous representations serve as conditioning inputs to the Distribution-Conditioned Diffusion Decoder, which refines localized visual structures to generate high-quality images. During training, instead of forwarding the VLM itself, the logits are approximated using the VQ-VAE Encoder from the VLM’s pre-training pipeline, followed by lightweight Logit Calibration to match the VLM’s logit distribution.

cally relevant codebook entries, indicating a selective and low-entropy belief over image tokens. In contrast, the raw similarity-based pseudo-logits from the VQ-VAE encoder tend to produce near-uniform, high-entropy distributions over the codebook, where a large number of tokens receive comparable probability mass.

This discrepancy is quantitatively analyzed in Table 1, which compares token-probability statistics and Otsu-derived thresholding results for the VLM logits and the VQ-VAE pseudo-logits. While the VLM’s distribution concentrates probability mass on a small set of dominant tokens, the encoder’s raw pseudo-logits exhibit flat distributions in which thousands of tokens are statistically indistinguishable. Such a mismatch implies that directly using discrete codes or uncalibrated encoder logits as diffusion-conditioning signals fails to reflect the semantic selectivity present in the VLM’s internal belief.

To bridge this gap, we apply a lightweight Logit Calibration that rescales and shifts the encoder-side similarity scores. This calibration aligns the entropy and peak behavior of the encoder distributions with those of the VLM logits, enabling distributionally consistent soft assignments over the codebook. By establishing a common continuous representation space between the VLM and the VQ-VAE encoder, this calibrated formulation provides a principled foundation for diffusion-based decoding that preserves the semantic intent encoded in the VLM’s token probabilities.

## 4. Method

Our goal is to enhance the visual fidelity of images generated by a pre-trained autoregressive vision-language model without modifying its architecture or training procedure. To this end, we introduce a diffusion-based decoder that reconstructs high-fidelity images directly from the VLM’s

**Table 1.** Token-probability statistics and Otsu thresholding results for the VLM’s image-token logits, the raw VQ-VAE pseudo-logits, and our calibrated pseudo-logits. The probability statistics (top rows) summarize the sharpness and entropy characteristics of each distribution, while the Otsu-derived quantities (bottom rows) identify the number of statistically significant codebook entries (threshold rank) and the corresponding probability mass. Details on the computation and interpretation are provided in Appendix A.

Statistic	VLM	VQ-VAE	VQ-VAE (Cal.)
<i>Probability Distribution Statistics</i>			
Top-1 Probability	0.221627	0.000151	0.222283
Top-2 Probability	0.100532	0.000145	0.064229
Normalized Entropy	0.415303	0.993630	0.424155
Tail Entropy	0.560794	0.993661	0.520536
<i>Otsu Thresholding Statistics</i>			
Threshold (prob.)	$6.24 \times 10^{-2}$	$6.66 \times 10^{-5}$	$6.38 \times 10^{-2}$
Threshold Rank	2	5767	2
Head Mass	0.322160	0.492722	0.286512

image-token predictions. The core challenge lies in bridging the discrete image-token of the VLM and the continuous conditioning space for the diffusion models. We address this challenge through three components: Logit-to-Code Distributional Mapping (LCDM), Logit Calibration (LC), and Distribution-Conditioned Diffusion Decoder (DCDD).

### 4.1. Logit-to-Code Distributional Mapping

Autoregressive VLMs generate images by predicting discrete image tokens, but their internal predictions are expressed as continuous logits over a learned codebook. Rather than introducing new representations, LCDM extracts and preserves this latent belief already present in the VLM. Given *Image-Token Logits*  $\mathbf{l}_i \in \mathbb{R}^K$  at each spatial position, we first obtain the corresponding probability distribution  $p_{i,k}$  via softmax. We then compute a *Distribution-Weighted Code Vector*  $\mathbf{v}_i = \sum_{k=1}^K p_{i,k} \mathbf{e}_k$ , which represents the expected *Codebook* embedding under

the VLM’s predicted distribution.

Importantly, this aggregation does not aim to increase expressive power beyond that of the VLM. Instead, it serves as the minimal representation-preserving operation required to retain the model’s belief over image tokens, avoiding the information loss induced by hard token selection. In this sense, LCDM directly reformulates the continuous token-level belief already encoded in the VLM into a form that can be effectively utilized by diffusion-based reconstruction.

To complement the expected embedding, we additionally extract a small set of *Uncertainty Features* from the same token distribution, specifically the maximum probability, the confidence margin, the adaptive top- $K$  probability mass, and the normalized tail entropy. These features are not introduced as independent semantic signals; rather, they provide concise descriptors of distributional concentration and dispersion that would otherwise be collapsed by the *Distribution-Weighted Code Vector* alone. Together, the *Distribution-Weighted Code Vector* and *Uncertainty Features* form the conditioning representation for diffusion-based reconstruction.

#### 4.2. Logit Calibration

During diffusion training, conditioning representations must be derived from ground-truth images rather than VLM-generated tokens. We therefore obtain *Proxy Image-Token Logits* from the VQ-VAE encoder used in the same tokenization pipeline. Although these logits are structurally aligned with the VLM’s codebook, their probability distributions differ significantly in entropy and confidence.

To bridge this train-inference gap, we apply a lightweight **Logit Calibration** procedure that aligns the encoder-side token distributions with the intrinsic statistics of the VLM. Calibration is performed by matching simple distributional summaries (maximum probability, the confidence margin, the adaptive top- $K$  probability mass, and the normalized tail entropy) computed from VLM-generated logits. This process introduces no additional learnable parameters in the VLM or diffusion model and ensures that training-time conditioning faithfully reflects inference-time behavior.

#### 4.3. Distribution-Conditioned Diffusion Decoder

Finally, a diffusion transformer reconstructs high-fidelity images conditioned on the calibrated continuous representations. The diffusion model operates in the latent space of a pre-trained VAE and is conditioned on the spatially arranged distribution-weighted code vectors and uncertainty features. Condition is injected through simple linear projections and additive fusion with noisy latent tokens, preserving architectural simplicity.

By design, our diffusion acts purely as a reconstruction

module. It does not reinterpret or override the semantics produced by the VLM, but instead realizes them with higher visual fidelity. To minimize semantic distortion, we exclude text information from the diffusion process and rely solely on the VLM-derived token representations as guidance.

A detailed formulation and implementation details of all three components are provided in Appendix B.

## 5. Experiments and Results

### 5.1. Training Data and Evaluation Metrics

We trained the diffusion-based decoder on the ImageNet-1K train set (Russakovsky et al., 2015), using the standard resize-center-crop preprocessing (Krizhevsky et al., 2012), and evaluated its performance on both image reconstruction and text-to-image generation. For reconstruction, we measured fidelity on the ImageNet-1K validation set and MJHQ-30K (Li et al., 2024a) using reconstruction FID (Heusel et al., 2017), SSIM (Wang et al., 2004), and LPIPS (Zhang et al., 2018), which assess overall generation quality, structural similarity, and perceptual distance, respectively. Our primary objective is to improve image fidelity given fixed semantic content produced by a pre-trained VLM, rather than to enhance text-image semantic alignment itself. Accordingly, we do not focus on extensive evaluation over text-to-image benchmarks that primarily emphasize semantic correctness or compositional reasoning. Nevertheless, to verify that our fidelity-oriented decoding does not introduce adverse side effects on semantic alignment, we additionally report the GenEval (Ghosh et al., 2023) correctness score for text-to-image generation. We further measure generation FID on MJHQ-30K to assess aesthetic fidelity under free-form generation.

### 5.2. Implementation Details

We finetune the FLUX.1-Fill diffusion transformer (Labs et al., 2025) as our image decoder. Only the transformer’s attention and adapter layers are updated, while remaining backbone parameters are kept frozen. Training is performed on four A100 (80GB) GPUs with mixed precision, a global batch size of 32, and 50K training steps for reported models. We use AdamW (Loshchilov & Hutter, 2017) with a learning rate of  $2 \times 10^{-5}$ . At inference, we perform 30 denoising steps, and the ablation study on the denoising steps are provided in the Appendix D. All other diffusion and VLM hyperparameters are kept consistent with the official FLUX.1-Fill and pre-trained model configurations.

For our method-specific components, we inherit the VQ-VAE tokenizer and codebook of the most recent publicly available pre-trained VLM, Janus-Pro 7B (Chen et al., 2025), with additional VLM backbone reported in the Appendix E. To obtain the Target Distribution Statistics, we generate 100

images from randomly sampled prompts. During calibration, the cosine-scale factor is searched over a range from 10 to 60, the label-smoothing value  $\epsilon$  is selected from a small grid around zero, and the affine scale  $a$  and bias  $b$  are adjusted within narrow neighborhoods of 1.0 and 0.0. Calibration is considered converged once the encoder’s mean normalized entropy matches that of the VLM within a tolerance of 0.02. Further implementation details can be found at Appendix C

### 5.3. Image Reconstruction

We first evaluate image reconstruction performance using the VQ-VAE tokenizer, comparing the baseline VQ-VAE decoder with our diffusion-based decoder. This experiment provides an upper bound on the image quality attainable through our decoder and directly reflects the training objective of our diffusion model. Quantitative results in Table 2 show that our method consistently improves reconstruction quality in all metrics, with particularly notable gains in reconstruction FID. This indicates that our decoder better preserves high-frequency visual realism, aligning closely with our core motivation. Improvements are observed not only on ImageNet, a real-world photographic domain on which the decoder is trained, but also on MJHQ-30K, a high-fidelity synthetic domain, demonstrating the strong cross-domain generalization ability of our approach. In contrast, SSIM and LPIPS remain relatively unchanged, which we attribute to the design of our method: it enhances fidelity while preserving the semantic structure encoded in the image tokens, thereby avoiding unintended semantic distortion of the VLM’s intended visual content. Qualitative comparisons are shown in Figure 1 and 8.

Table 2. **Quantitative Results on Image Reconstruction.** We evaluate image reconstruction on ImageNet-1K and MJHQ-30K, reporting metrics averaged across all classes and categories. It compares the baseline VLM’s native VQ-VAE decoder and our diffusion-based decoder, evaluated with the recent publicly available Janus-Pro 7B ( $384 \times 384$ ) backbone. Results for additional VLM backbones, along with ablation studies analyzing each of our component’s effect on performance, are provided in the **Supplementary**. Superior results are **highlighted**.

<i>ImageNet-1K Val.</i>	rFID↓	SSIM↑	LPIPS↓
VQ-VAE Decoder	2.8511	0.5786	0.1541
<b>LCDM+LC+DCDD (ours)</b>	<b>0.7535</b>	<b>0.5957</b>	<b>0.1374</b>
<i>MJHQ-30K</i>	rFID↓	SSIM↑	LPIPS↓
VQ-VAE Decoder	4.4882	0.6564	0.1432
<b>LCDM+LC+DCDD (ours)</b>	<b>1.8127</b>	<b>0.6782</b>	<b>0.1308</b>

### 5.4. Text-to-Image Generation

We evaluate aesthetic and perceptual quality on the MJHQ-30K benchmark. As shown in Table 3, our method yields substantial improvements across nearly all categories, con-

firmed that our VQ-VAE–encoder–based training strategy with Logit Calibration generalizes effectively to the VLM’s inference-time token distributions.

To assess whether fidelity-driven enhancements influence text–image compositional behavior, we additionally report GenEval scores. Although our method does not alter the semantics encoded by the VLM’s predicted tokens, we observe clear improvements in the *Single*, *Two*, and *Counting* categories. These tasks depend primarily on the detectability and separability of object-level features rather than on semantic modification, indicating that higher-fidelity generation makes object shapes, boundaries, and local attributes easier for automated detectors to identify. Categories such as *Position*, which rely on spatial reasoning rather than appearance-level cues, show limited change, consistent with our semantic-preserving design. Overall, these findings indicate that enhancing visual fidelity not only improves perceptual quality but also brings incidental gains in compositional correctness, even without explicit optimization for text-to-image alignment. Qualitative examples are shown in Figure 5 and 9.

## 6. Ablation Studies

### 6.1. Effect of Our Components

To isolate the effect of each component in our framework, we conduct an ablation study using three diffusion models trained with three different conditioning representations. Since our components can operate on fundamentally different forms of conditioning, ranging from discrete code indices to calibrated continuous distribution-weighted embeddings, a fair comparison requires training a dedicated diffusion model for each representation. All ablation models are trained for 10K steps under identical optimization settings and evaluated on the ImageNet-1K validation set using the image reconstruction protocol.

We compare the following variants:

1. **Diffusion Decoder (Baseline)**, which conditions the FLUX.1-Fill-based diffusion decoder on discrete VQ code vectors, using the same architecture as the Distribution-Conditioned Diffusion Decoder (DCDD);
2. **DCDD+LCDM**, which replaces discrete conditioning with continuous distribution-weighted code embeddings obtained via Logit-to-Code Distributional Mapping (LCDM);
3. **DCDD+LCDM+LC**, which additionally applies Logit Calibration (LC) to align the encoder-side conditioning distribution with the VLM’s token-logit statistics.

Qualitative and quantitative comparisons are presented in Figure 4 and Table 4. Introducing LCDM improves

## High-Fidelity T2I Generation from Pre-Trained VLM via Distribution-Conditioned Diffusion Decoding

Table 3. **Quantitative results on text-to-image generation.** We evaluate MJHQ-30K and GenEval metrics, respectively: MJHQ measures generation FID (lower is better), while GenEval assesses semantic correctness across object existence, attributes, counting, and spatial relations (higher is better). Results of the Janus-Pro 7B backbone are reported, and additional VLM backbones are provided in the **Supplementary**. Superior results are **highlighted**.

<b>MJHQ-30K</b>	Overall	Animals	Art	Fashion	Food	Indoor	Landscape	Logo	People	Plants	Vehicles
VQ-VAE Decoder	14.2888	31.6866	35.6408	32.1410	33.1787	32.4016	30.5020	42.3565	37.6049	33.1228	27.4424
<b>LCDM+LC+DCDD (ours)</b>	<b>9.4160</b>	<b>25.1060</b>	<b>28.9806</b>	<b>26.0182</b>	<b>28.1580</b>	<b>28.5172</b>	<b>26.7104</b>	<b>38.2032</b>	<b>30.2217</b>	33.6617	<b>25.0277</b>

<b>GenEval</b>	Overall	Single	Two	Counting	Colors	Position	Color Attr.
VQ-VAE Decoder	77.24	97.81	84.09	56.56	87.50	75.75	61.75
<b>LCDM+LC+DCDD (ours)</b>	<b>78.31</b>	<b>99.06</b>	<b>88.89</b>	<b>59.38</b>	<b>88.30</b>	72.50	61.75

Table 4. Quantitative ablation results on ImageNet-1K image reconstruction. Each row corresponds to a diffusion model trained with a different conditioning representation. The best performance for each metric is **highlighted**.

<b>ImageNet-1K Val.</b>	rFID↓	SSIM↑	LPIPS↓
<i>Diff. Dec. (baseline)</i>	33.5081	0.4244	0.4132
<b>DCDD+LCDM</b>	31.2049	0.4275	0.4009
<b>DCDD+LCDM+LC</b>	<b>30.5760</b>	<b>0.4360</b>	<b>0.3875</b>

the structural correspondence between reconstructions and ground-truth images, indicating that continuous distribution-weighted conditioning better preserves fine-grained spatial details. However, when the conditioning distributions used during training and inference are mismatched, LCDM alone tends to amplify color contrast and introduce mild noise artifacts.

Incorporating LC effectively regularizes the conditioning distribution, mitigating the contrast inflation and suppressing noise artifacts caused by uncalibrated token probabilities. As a result, reconstructions exhibit stable color tones and improved visual consistency.

These trends are consistently reflected across all three evaluation metrics. LPIPS decreases monotonically across variants, suggesting that both LCDM and LC contribute to improved perceptual coherence and texture quality. Reconstruction FID benefits primarily from LCDM, as continuous distribution-weighted embeddings yield global feature statistics closer to those of real images. In contrast, SSIM improves more substantially with LC, since calibration reduces color drift and contrast variability, thereby restoring local luminance stability and structural consistency.

Overall, these results indicate that the gains of our approach do not stem solely from the expressive capacity of a strong diffusion backbone. Instead, they arise from the complementary effects of continuous conditioning via LCDM and statistical alignment through LC.

### 6.2. Computational Cost

Our method provides an optional diffusion-based decoding pathway that can serve as an alternative to the native VQ-VAE decoder of a pre-trained autoregressive VLM, enabling

higher-fidelity image synthesis while keeping the VLM entirely fixed. Although the diffusion decoder introduces iterative denoising steps (30 diffusion steps in our setting) and thus incurs additional computation when considered in isolation, the end-to-end text-to-image cost remains dominated by the autoregressive VLM. As a result, the overall increase in generation cost is moderate.

Table 5 summarizes the end-to-end performance-latency trade-off on the MJHQ-30K text-to-image benchmark. Despite increasing end-to-end latency by 31%, our approach yields a 34% improvement in gFID, indicating a substantial gain in generation fidelity. Importantly, in our framework, the diffusion decoder is an optional component: it can be selectively enabled when high visual fidelity is desired, or bypassed to retain the original VQ-VAE decoding path when computational efficiency is prioritized. This flexibility allows our framework to adapt to different usage scenarios while maintaining a favorable quality-latency trade-off.

From a computational perspective, our approach increases inference-time FLOPs due to the additional denoising steps of the diffusion decoder. However, this cost is confined to the decoding stage and is incurred only when the diffusion pathway is enabled. Crucially, our framework completely avoids retraining the pre-trained VLM, and the diffusion decoder itself can be trained efficiently using a relatively small dataset and a short training schedule. As a result, the increased inference cost is offset by a substantial reduction in training-time computational resources, while preserving the full representational capacity and learned behavior of the original pre-trained VLM.

Table 5. End-to-end text-to-image comparison between our method and the baseline on the MJHQ-30K benchmark with Janus-Pro 7B. Using 30 denoising diffusion steps, our diffusion-based decoder achieves 34% lower FID while increasing end-to-end latency by only 31%.

<b>Janus-Pro 7B</b>		
<b>MJHQ-30K Benchmark</b>	gFID↓	Latency (s)↓
Baseline (VLM + VQ-VAE)	14.28	11.86
Ours (VLM + Diffusion)	9.41	15.56
Trade-off	<b>-34.12%</b>	<b>+31.19%</b>

## 7. Conclusion

We presented a diffusion-based decoding framework that substantially improves the visual fidelity of pre-trained VLM without modifying or retraining the VLM itself. By introducing our Logit-to-Code Distributional Mapping and Logit Calibration, our Distribution-Conditioned Diffusion Decoder effectively aligns training-time proxy logits with the VLM’s inference-time distributions and achieves strong gains in both reconstruction and text-to-image generation after short training on ImageNet-1K.



Figure 4. Ablation results comparing the effect of discrete conditioning (*Diff. Dec. (baseline)*), continuous distribution-weighted conditioning (*DCDD+LCDM*), and calibrated continuous conditioning (*DCDD+LCDM+LC*) on ImageNet-1K image reconstruction.



Figure 5. Qualitative results on text-to-image generation. Comparison between images decoded from the VLM’s predicted tokens using its native VQ-VAE decoder and our diffusion-based decoder on prompts from the MJHQ-30K benchmark. Additional samples with corresponding prompts are provided in the Appendix.

## Impact Statement

This work aims to advance the field of machine learning by improving the visual fidelity of text-to-image generation. As with other advances in image generation, the proposed method could contribute to the creation of highly realistic synthetic images, which may raise concerns related to misuse, such as the generation of misleading or deceptive visual content. These risks are not unique to our approach and are inherent to the broader class of generative image models; established safeguards and responsible use practices developed for generative AI remain applicable. Overall, we believe that the societal implications of this work align with those already recognized in the advancement of generative machine learning systems.

## References

- Chen, X., Wu, Z., Liu, X., Pan, Z., Liu, W., Xie, Z., Yu, X., and Ruan, C. Janus-pro: Unified multimodal understanding and generation with data and model scaling. *arXiv preprint arXiv:2501.17811*, 2025.
- Esser, P., Rombach, R., and Ommer, B. Taming transformers for high-resolution image synthesis. In *Proceedings of the IEEE/CVF conference on computer vision and pattern recognition*, pp. 12873–12883, 2021.
- Geng, Z., Wang, Y., Ma, Y., Li, C., Rao, Y., Gu, S., Zhong, Z., Lu, Q., Hu, H., Zhang, X., et al. X-omni: Reinforcement learning makes discrete autoregressive image generative models great again. *arXiv preprint arXiv:2507.22058*, 2025.
- Ghosh, D., Hajishirzi, H., and Schmidt, L. Geneval: An object-focused framework for evaluating text-to-image alignment. *Advances in Neural Information Processing Systems*, 36:52132–52152, 2023.
- Heusel, M., Ramsauer, H., Unterthiner, T., Nessler, B., and Hochreiter, S. Gans trained by a two time-scale update rule converge to a local nash equilibrium. *Advances in neural information processing systems*, 30, 2017.
- Huang, R., Wang, C., Yang, J., Lu, G., Yuan, Y., Han, J., Hou, L., Zhang, W., Hong, L., Zhao, H., et al. Illume+: Illuminating unified mllm with dual visual tokenization and diffusion refinement. *arXiv preprint arXiv:2504.01934*, 2025.
- Kingma, D. and Gao, R. Understanding diffusion objectives as the elbo with simple data augmentation. *Advances in Neural Information Processing Systems*, 36:65484–65516, 2023.
- Krizhevsky, A., Sutskever, I., and Hinton, G. E. Imagenet classification with deep convolutional neural networks. *Advances in neural information processing systems*, 25, 2012.
- Labs, B. F., Batifol, S., Blattmann, A., Boesel, F., Consul, S., Diagne, C., Dockhorn, T., English, J., English, Z., Esser, P., Kulal, S., Lacey, K., Levi, Y., Li, C., Lorenz, D., Müller, J., Podell, D., Rombach, R., Saini, H., Sauer, A., and Smith, L. Flux.1 kontext: Flow matching for in-context image generation and editing in latent space, 2025. URL <https://arxiv.org/abs/2506.15742>.
- Li, D., Kamko, A., Akhgari, E., Sabet, A., Xu, L., and Doshi, S. Playground v2.5: Three insights towards enhancing aesthetic quality in text-to-image generation, 2024a.
- Li, K., Brack, M., Katakol, S., Ravi, H., and Kale, A. Unifusion: Vision-language model as unified encoder in image generation. *arXiv preprint arXiv:2510.12789*, 2025.
- Li, T., Tian, Y., Li, H., Deng, M., and He, K. Autoregressive image generation without vector quantization. *Advances in Neural Information Processing Systems*, 37:56424–56445, 2024b.
- Loshchilov, I. and Hutter, F. Decoupled weight decay regularization. *arXiv preprint arXiv:1711.05101*, 2017.
- Russakovsky, O., Deng, J., Su, H., Krause, J., Satheesh, S., Ma, S., Huang, Z., Karpathy, A., Khosla, A., Bernstein, M., Berg, A. C., and Fei-Fei, L. ImageNet Large Scale Visual Recognition Challenge. *International Journal of Computer Vision (IJCV)*, 115(3):211–252, 2015. doi: 10.1007/s11263-015-0816-y.
- Sun, P., Jiang, Y., Chen, S., Zhang, S., Peng, B., Luo, P., and Yuan, Z. Autoregressive model beats diffusion: Llama for scalable image generation. *arXiv preprint arXiv:2406.06525*, 2024.
- Tang, H., Wu, Y., Yang, S., Xie, E., Chen, J., Chen, J., Zhang, Z., Cai, H., Lu, Y., and Han, S. Hart: Efficient visual generation with hybrid autoregressive transformer. *arXiv preprint arXiv:2410.10812*, 2024.
- Van Den Oord, A., Vinyals, O., et al. Neural discrete representation learning. *Advances in neural information processing systems*, 30, 2017.
- Wang, Y., Lin, Z., Teng, Y., Zhu, Y., Ren, S., Feng, J., and Liu, X. Bridging continuous and discrete tokens for autoregressive visual generation. *arXiv preprint arXiv:2503.16430*, 2025.
- Wang, Z., Bovik, A. C., Sheikh, H. R., and Simoncelli, E. P. Image quality assessment: from error visibility to structural similarity. *IEEE transactions on image processing*, 13(4):600–612, 2004.

Wu, Y., Cai, H., Chen, J., Zhang, Z., Xie, E., Yu, J., Chen, J., Hu, J., Lu, Y., and Han, S. Dc-ar: Efficient masked autoregressive image generation with deep compression hybrid tokenizer. In *Proceedings of the IEEE/CVF International Conference on Computer Vision*, pp. 18034–18045, 2025.

Xie, J., Mao, W., Bai, Z., Zhang, D. J., Wang, W., Lin, K. Q., Gu, Y., Chen, Z., Yang, Z., and Shou, M. Z. Show-o: One single transformer to unify multimodal understanding and generation. *arXiv preprint arXiv:2408.12528*, 2024.

Zhang, R., Isola, P., Efros, A. A., Shechtman, E., and Wang, O. The unreasonable effectiveness of deep features as a perceptual metric. In *Proceedings of the IEEE conference on computer vision and pattern recognition*, pp. 586–595, 2018.

## A. Extended Conceptual Motivation

To assess whether replacing discrete VQ code vector with continuous distribution-weighted code vector is statistically justified, we first analyze the probability distribution of image-token logits produced by the VLM in Table 1. We apply Otsu’s thresholding, a classical variance-minimization method that partitions a probability sequence into statistically meaningful “foreground” and “background” components by selecting the threshold that maximizes inter-class variance. Given sorted probabilities  $\{p_{(1)}, \dots, p_{(K)}\}$ , the optimal threshold  $\tau^*$  is obtained by

$$\begin{aligned} \tau^* &= \arg \max_{\tau} \sigma_{\text{between}}^2(\tau) \\ &= \omega_0(\tau) \omega_1(\tau) (\mu_0(\tau) - \mu_1(\tau))^2, \end{aligned} \quad (1)$$

where  $\omega_c$  and  $\mu_c$  denote the total mass and mean of each partition, respectively.

The left column of Table 1 shows that for our baseline VLM, Janus-Pro 7B, Otsu’s threshold yields a rank of 2, indicating that at least two codebook vectors carry statistically meaningful probability mass. Although the VLM ultimately samples a single discrete token during autoregressive decoding, this analysis reveals that the true underlying token distribution is not strictly one-hot and that relying solely on the top-1 index discards semantically relevant information. To preserve this informative probability distribution in the diffusion conditioning, we adopt our Logit-to-Code Distributional Mapping (LCDM) which forms continuous embeddings via a probability-weighted expectation over the codebook.

In contrast, the VQ-VAE encoder produces extremely flat pseudo-logit distributions, with an Otsu threshold rank of 5,767 shown at the middle column of Table 1. This behavior can be explained analytically. The codebook size is large,  $K = 16,384$ , and the raw cosine-similarity logits typically lie within a narrow numerical range, roughly  $[-1, 1]$ . Approximating the maximum logit as 1 and the remaining logits near 0, the softmax yields

$$p_{\max} \approx \frac{e^1}{e^1 + (K-1)e^0} \approx 1.6 \times 10^{-4}, \quad (2)$$

while all non-max tokens obtain probabilities near

$$p_{\text{others}} \approx \frac{1}{K} \approx 6.1 \times 10^{-5}. \quad (3)$$

Thus even the top token is only slightly larger than the uniform baseline, making the pseudo-logit distribution appear nearly flat. With such a high-entropy distribution, thousands of tokens surpass Otsu’s threshold, indicating that the encoder’s logits fail to capture the sharp semantic selectivity present in the VLM.

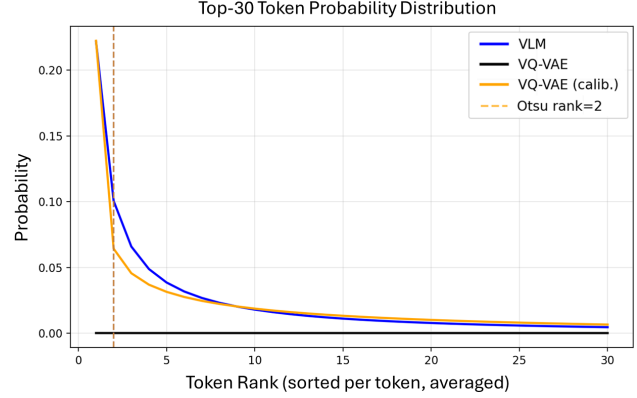


Figure 6. Average top-30 token probability distributions for Janus-Pro 7B (VLM), the VQ-VAE encoder, and the calibrated VQ-VAE encoder. Each curve visualizes per-token probabilities sorted by rank and then averaged across 100 images. The dashed line marks the Otsu-derived threshold rank.

This mismatch implies that directly using discrete codes or raw VQ-VAE logits as diffusion-conditioning signals discards meaningful information carried in the VLM’s token probabilities. This motivates the use of our **Logit Calibration**.

Using the *Target Distribution Statistics* obtained from our VLM logit analysis, we calibrate the VQ-VAE pseudo logits to match the statistical behavior of the VLM’s token distributions. As shown in the right column of Table 1, calibration substantially restores the desired sharpness. The Otsu threshold rank becomes 2, identical to that of the VLM, and the top-1 probability and the head mass closely matches the VLM’s value. This demonstrates that our calibration reshapes the pseudo-logit distribution into one that faithfully reproduces the semantic selectivity exhibited by the VLM.

Figure 6 visualizes the average top-30 probability distribution across 100 images for the VLM, the uncalibrated VQ-VAE encoder, and the calibrated encoder. The calibrated probabilities closely follow the VLM’s decay pattern, whereas the uncalibrated encoder yields an overly flat distribution. These results confirm that our LC is essential for enabling LCDM to operate on probability distributions that faithfully reflect the VLM’s semantic token structure, thereby reducing the discrepancy between training-time conditioning via VQ-VAE and the inference-time conditioning via VLM.

## B. Extended Method Details

### B.1. Logit-to-Code Distributional Mapping

This stage transforms the discrete tokens generated from a pre-trained autoregressive VLM into continuous conditioning representations that enrich the diffusion decoder with dense, fine-grained visual information for high-fidelity

image synthesis.

Given either the *Image-Token Logits* from the VLM during inference or the *Proxy Image-Token Logits* derived from the VQ-VAE encoder during training, this mapping converts these logits into two key representations: the ***Distribution-Weighted Code Vector*** capturing the expected semantic embedding per token, and the complementary ***Uncertainty Features*** quantifying confidence and ambiguity in token prediction.

### Inference with VLM:

During inference, the autoregressive VLM produces a sequence of *Image-Token Logits*

$$\mathbf{L} = [\mathbf{l}_1, \dots, \mathbf{l}_N] \in \mathbb{R}^{N \times K}, \quad (4)$$

where  $N$  denotes the number of image tokens and  $K$  the size of the visual codebook. Each  $\mathbf{l}_i = [l_{i,1}, \dots, l_{i,K}]$  represents the similarity between the model’s hidden representation and the  $K$  learned ***Code Vectors***  $\mathcal{E} = \{\mathbf{e}_1, \dots, \mathbf{e}_K\}$  with  $\mathbf{e}_k \in \mathbb{R}^D$ . In practice, the logits may be obtained after applying classifier-free guidance and/or temperature scaling; for notational simplicity, we omit these operators and write the resulting distribution in a standard softmax form.

The logits are transformed into normalized *Image-Token Probabilities* via a standard softmax:

$$p_{i,k} = \frac{\exp(l_{i,k})}{\sum_{j=1}^K \exp(l_{i,j})}, \quad \mathbf{P} = [p_{i,k}] \in \mathbb{R}^{N \times K}. \quad (5)$$

Each row of  $\mathbf{P}$  represents the probability distribution over the  $K$  codebook entries for a specific spatial token position. To convert these discrete distributions into continuous embeddings, each probability vector  $\mathbf{p}_i \in \mathbb{R}^K$  is used to compute a weighted combination of the corresponding ***Code Vectors*** in the codebook  $\mathbf{E} = [\mathbf{e}_1; \dots; \mathbf{e}_K] \in \mathbb{R}^{K \times D}$ :

$$\mathbf{v}_i = \sum_{k=1}^K p_{i,k} \mathbf{e}_k, \quad \mathbf{v}_i \in \mathbb{R}^D. \quad (6)$$

Stacking all token embeddings yields the matrix form:

$$\mathbf{V} = \mathbf{P} \mathbf{E} \in \mathbb{R}^{N \times D}. \quad (7)$$

This operation performs a probability-weighted aggregation of the codebook features, projecting each token’s probability distribution  $\mathbf{p}_i$  into the continuous latent space of the VQ-VAE codebook. The resulting ***Distribution-Weighted Code Vectors***  $\mathbf{V}$  serve as dense and information-rich representations that preserve the fine-grained semantic information contained in the VLM’s predictions.

However, this weighted aggregation inherently compresses each token’s probability distribution into a single expectation, discarding information about its sharpness and variability. To compensate for this loss and explicitly capture

the model’s confidence and ambiguity, we derive four scalar statistics from  $\mathbf{P}$  for each spatial token  $i$ :

$$\begin{aligned} u_i^{(1)} &= \max_k p_{i,k} && \text{(confidence),} \\ u_i^{(2)} &= p_{i,(1)} - p_{i,(2)} && \text{(margin),} \\ u_i^{(3)} &= \sum_{k \in \text{Top-}K_u} p_{i,k} && \text{(top-}K_u \text{ mass),} \\ u_i^{(4)} &= -\frac{\sum_{k \neq k^*} p_{i,k} \log p_{i,k}}{\log(K-1)} && \text{(tail entropy),} \end{aligned} \quad (8)$$

where  $p_{i,(1)}$  and  $p_{i,(2)}$  denote the top-1 and top-2 probabilities, and  $k^* = \arg \max_k p_{i,k}$ . For the top- $K_u$  mass, we employ an entropy-adaptive  $K_u$  constrained between 8 and 64 tokens, ensuring that the statistic reflects an appropriate portion of the probability mass across varying distribution sharpness. These measures are concatenated into ***Uncertainty Features***  $\mathbf{U} \in \mathbb{R}^{N \times 4}$ , which complement the continuous code representations  $\mathbf{V}$  by summarizing the dispersion characteristics of each token’s probability distribution. Together,  $(\mathbf{V}, \mathbf{U})$  provide the diffusion decoder with both semantic and confidence-aware information for localized refinement.

### Training with VQ-VAE Encoder:

During training, we generate *Proxy Image-Token Logits* using the ***VQ-VAE encoder*** employed in the same visual tokenization pipeline as the target VLM. Given a ground-truth image  $x \in \mathbb{R}^{3 \times H \times W}$ , the VQ-VAE encoder downsamples the image through a series of convolutional and residual blocks, producing spatial latent features immediately before vector quantization. These latent features, referred to as ***Image-Token Features***  $\mathbf{F}$ , capture compact yet semantically rich representations of local regions, encoding their color, texture, and structural patterns. Thus, we obtain

$$\mathbf{F} = [\mathbf{f}_1, \dots, \mathbf{f}_N] \in \mathbb{R}^{N \times D}, \quad (9)$$

from the encoder, where  $N$  is the number of spatial tokens and  $D$  is the feature dimension.

Each feature  $\mathbf{f}_i$  is then compared with all entries in the learned ***Codebook***  $\mathcal{E} = \{\mathbf{e}_1, \dots, \mathbf{e}_K\}$  with  $\mathbf{e}_k \in \mathbb{R}^D$  to produce *Proxy Image-Token Logits*:

$$s_{i,k} = \text{sim}(\mathbf{f}_i, \mathbf{e}_k), \quad \mathbf{S} = [s_{i,k}] \in \mathbb{R}^{N \times K}, \quad (10)$$

where  $\text{sim}(\cdot, \cdot)$  denotes a cosine similarity measure.

We then apply the same LCDM transform as in inference (Eqs. (5)–(8)) to obtain the ***Distribution-Weighted Code Vectors*** and ***Uncertainty Features*** for diffusion conditioning:

$$\mathbf{V}^{\text{enc}} = \mathbf{P}^{\text{enc}} \mathbf{E} \in \mathbb{R}^{N \times D}, \quad \mathbf{U}^{\text{enc}} \in \mathbb{R}^{N \times 4}.$$

For diffusion training, it is essential to establish explicit correspondence between each ground-truth image and its

conditioning representation. The above process enables this by constructing *Proxy Image-Token Logits* that closely align with the inference-time outputs of the VLM. Although these proxy logits contain the same structural semantics and codebook alignment as the VLM’s generated logits, their probability distributions may diverge, leading to a potential train–inference gap. To mitigate this mismatch, we apply **Logit Calibration**, as described in the following section.

## B.2. Logit Calibration

Although the VQ-VAE encoder produces structurally aligned *Proxy Image-Token Logits* via feature-to-code similarity, their statistical behavior differs significantly from that of the pre-trained VLM. In particular, the encoder’s similarity-based logits tend to exhibit substantially higher entropy and weaker confidence than the VLM’s image-token logits, which encode a selective belief over a small set of semantically relevant codebook entries. To bridge this discrepancy, we introduce a **Logit Calibration** procedure that aligns the encoder’s token-probability distribution with the VLM’s intrinsic confidence and entropy characteristics.

**Target Distribution Statistics.** We first estimate the *Target Distribution Statistics* of the VLM by sampling the pre-trained text-to-image model over a set of random prompts. Specifically, we draw  $N = 100$  prompts from the GenEval benchmark and generate  $T = 576$  image tokens per prompt using classifier-free guidance with weight  $w_{\text{cfg}} = 5.0$  and temperature  $\tau_{\text{VLM}} = 1.0$ . For each decoding step, we obtain the guided image-token distribution  $p^{\text{VLM}}(\cdot)$  and compute its token-level confidence  $\max_k p_k$  and normalized entropy

$$H_{\text{norm}}(p) = -\frac{1}{\log K} \sum_{k=1}^K p_k \log p_k, \quad (11)$$

where  $K = 16,384$  is the size of the image-token vocabulary. Aggregating these quantities across all  $N \times T$  tokens yields the VLM’s target statistics

$$\mathcal{T}_{\text{VLM}} = (\mu_H, \mu_C, P_{95}(C), P_{95}(H)), \quad (12)$$

where  $\mu_H$  and  $P_{95}(H)$  denote the mean and 95th-percentile entropy, and  $\mu_C$  and  $P_{95}(C)$  denote the corresponding confidence statistics.

**Encoder Logits and Calibration Transform.** On the encoder side, we evaluate the VQ-VAE encoder on a set of  $M = 100$  training images. For each latent image-token feature  $\mathbf{f}_i \in \mathbb{R}^D$ , the encoder computes cosine similarity logits

$$s_{i,k} = \cos(\mathbf{f}_i, \mathbf{e}_k), \quad (13)$$

where  $\mathbf{e}_k \in \mathbb{R}^D$  denotes the  $k$ -th codebook vector. These similarity-based logits are then transformed via an affine

scaling and temperature-controlled softmax:

$$\tilde{s}_{i,k} = a s_{i,k} + b, \quad p_{i,k}^{\text{enc}} = \frac{\exp(\tilde{s}_{i,k}/\alpha)}{\sum_{j=1}^K \exp(\tilde{s}_{i,j}/\alpha)}, \quad (14)$$

where  $a$  and  $b$  denote the global logit scale and affine bias, and  $\alpha$  controls the sharpness of the distribution. After softmax, we apply label smoothing

$$\hat{p}_{i,k} = (1 - \epsilon) p_{i,k}^{\text{enc}} + \frac{\epsilon}{K}, \quad (15)$$

which mitigates overconfident predictions and stabilizes the tail behavior of the distribution.

**Calibration Objective and Optimization.** From the calibrated encoder distributions  $\hat{p}_{i,k}$ , we compute the corresponding entropy and confidence statistics  $\mu_H^{\text{enc}}, \mu_C^{\text{enc}}, P_{95}(C)^{\text{enc}}, P_{95}(H)^{\text{enc}}$  and match them to the VLM’s target statistics in Eq. (12). To quantify the mismatch, we define the weighted objective

$$\begin{aligned} \mathcal{L}(\theta) = & w_1(\mu_H^{\text{enc}} - \mu_H)^2 + w_2(\mu_C^{\text{enc}} - \mu_C)^2 \\ & + w_3(P_{95}(C)^{\text{enc}} - P_{95}(C))^2 \\ & + w_4(P_{95}(H)^{\text{enc}} - P_{95}(H))^2, \end{aligned} \quad (16)$$

where  $\theta = (a, b, \alpha, \epsilon)$  and  $(w_1, w_2, w_3, w_4) = (1.0, 0.25, 0.25, 0.35)$ . We prioritize matching the mean entropy, which provides the most reliable characterization of distributional sharpness, while confidence-based terms serve as secondary constraints.

The calibration parameters are determined via a coordinated, gradient-free search. We first tune the primary sharpness parameter  $a$  over  $[1, 60]$  using bisection until the encoder’s mean entropy satisfies  $|\mu_H^{\text{enc}} - \mu_H| \leq 0.02$ , fixing  $(b, \alpha, \epsilon) = (0, 1.0, 0)$ . Next, we sweep  $\alpha \in [0.5, 2.0]$  to refine the distribution’s softness, followed by a search over  $\epsilon \in [0.0, 0.05]$  to align the 95th-percentile confidence. Finally, we sweep the affine bias  $b \in [-0.10, 0.10]$  to correct residual offset mismatch and minimize the remaining discrepancy across all statistics.

For Janus-Pro 7B, the final calibrated configuration is  $a = 29.0381$ ,  $b = 0.0$ ,  $\alpha = 1.0$ , and  $\epsilon = 0.01$ . For consistency between training and inference, the same calibration, including mild label smoothing, is also applied to the VLM’s image-token logits during generation.

## B.3. Distribution-Conditioned Diffusion Decoder

The proposed diffusion decoder reconstructs high-fidelity images conditioned on the continuous token representations obtained from the LCDM stage. Given a ground-truth image  $x \in \mathbb{R}^{3 \times H \times W}$ , where  $H$  and  $W$  denote the height and width of the image, the diffusion model operates in the latent space

of a pre-trained VAE encoder:

$$\mathbf{z}_{\text{img}} = \text{VAE}_{\text{enc}}(x), \quad \mathbf{z}_{\text{img}} \in \mathbb{R}^{H' \times W' \times D_z}, \quad (17)$$

where  $H'$  and  $W'$  are the spatial dimensions of the latent feature map, and  $D_z$  is the latent channel dimension.

Noise is added according to a timestep-dependent variance schedule:

$$\tilde{\mathbf{z}}_{\text{img},t} = (1 - \sigma_t) \mathbf{z}_{\text{img}} + \sigma_t \boldsymbol{\epsilon}, \quad \boldsymbol{\epsilon} \sim \mathcal{N}(\mathbf{0}, \mathbf{I}), \quad (18)$$

where  $\sigma_t$  is the noise variance coefficient at timestep  $t$ ,  $\boldsymbol{\epsilon}$  represents standard Gaussian noise with zero mean and unit variance, and  $\tilde{\mathbf{z}}_{\text{img},t}$  denotes the noisy latent.

For conditioning, the **Distribution-Weighted Code Vectors**  $\mathbf{V}^{\text{enc}} \in \mathbb{R}^{N \times D}$  and the corresponding **Uncertainty Features**  $\mathbf{U}^{\text{enc}} \in \mathbb{R}^{N \times 4}$  are spatially reshaped and interpolated to match the latent resolution  $(H'/2, W'/2)$ . Here,  $N$  is the number of spatial tokens in the code representation, and each token has feature dimension  $D$ .

The code vectors are first linearly projected and then refined through a lightweight convolutional layer:

$$\mathbf{H}_{\text{code}} = \phi_{\text{conv}}(\text{Linear}(\mathbf{V}^{\text{enc}})), \quad \mathbf{H}_{\text{code}} \in \mathbb{R}^{N \times D_h}. \quad (19)$$

The function  $\text{Linear}(\cdot)$  is a fully connected layer that maps each code vector from  $\mathbb{R}^D$  to a hidden dimension  $\mathbb{R}^{D_h}$ , aligning its feature dimension with the diffusion model input. The operation  $\phi_{\text{conv}}(\cdot)$  denotes a  $3 \times 3$  convolution with normalization and activation, enhancing local spatial coherence among neighboring tokens.

The uncertainty features  $\mathbf{U}^{\text{enc}}$  are bilinearly upsampled to the same spatial resolution and concatenated channel-wise with the refined code features, forming the conditioning tensor:

$$\mathbf{C} = [\mathbf{H}_{\text{code}}, \mathbf{U}^{\text{enc}}], \quad \mathbf{C} \in \mathbb{R}^{N' \times (D_h + 4)}, \quad (20)$$

where  $N'$  corresponds to the number of spatial tokens after interpolation.

The noisy latent  $\tilde{\mathbf{z}}_{\text{img},t}$  is then divided into patch tokens and projected into the transformer feature space:

$$\mathbf{H}_{\text{img}} = \text{Proj}_{\text{img}}(\text{Pack}(\tilde{\mathbf{z}}_{\text{img},t})), \quad \mathbf{H}_{\text{img}} \in \mathbb{R}^{N' \times D_\theta}, \quad (21)$$

$$\mathbf{H}_{\text{cond}} = \text{Proj}_{\text{cond}}(\mathbf{C}), \quad \mathbf{H}_{\text{cond}} \in \mathbb{R}^{N' \times D_\theta}, \quad (22)$$

where  $\text{Pack}(\cdot)$  flattens the latent map into a sequence of  $N'$  spatial tokens, and  $\text{Proj}_{\text{img}}(\cdot)$  and  $\text{Proj}_{\text{cond}}(\cdot)$  are learned linear projections mapping the respective features into the transformer’s internal feature dimension  $D_\theta$ .

Two representations are fused by element-wise addition:

$$\mathbf{H}_{\text{input}} = \mathbf{H}_{\text{img}} + \mathbf{H}_{\text{cond}}, \quad \mathbf{H}_{\text{input}} \in \mathbb{R}^{N' \times D_\theta}. \quad (23)$$

The fused token representation is then processed by the diffusion transformer, producing token-wise output features:

$$\mathbf{H}_{\text{out}}^t = \mathcal{D}_\theta(\mathbf{H}_{\text{input}}, t), \quad \mathbf{H}_{\text{out}}^t \in \mathbb{R}^{N' \times D_\theta}, \quad (24)$$

where  $\mathcal{D}_\theta$  denotes the diffusion transformer parameterized by  $\theta$ .

Finally, the output token features are projected back to the latent channel dimension and reshaped into the spatial latent form to predict the residual velocity:

$$\hat{\mathbf{v}}^t = \text{Unpack}(\text{Proj}_{\text{out}}(\mathbf{H}_{\text{out}}^t)), \quad \hat{\mathbf{v}}^t \in \mathbb{R}^{H' \times W' \times D_z}, \quad (25)$$

where  $\text{Proj}_{\text{out}}(\cdot)$  denotes a learned linear projection to the latent dimension  $D_z$ , and  $\text{Unpack}(\cdot)$  reshapes the token sequence back into a spatial latent map of resolution  $H' \times W'$ .

The model is trained using the v-prediction objective (Kingma & Gao, 2023):

$$\mathcal{L}_{\text{v-pred}} = \mathbb{E}_t \left[ \|\mathbf{w}_t \cdot (\hat{\mathbf{v}}^t - (\boldsymbol{\epsilon} - \mathbf{z}_{\text{img}}))\|_2^2 \right], \quad (26)$$

where  $\mathbf{w}_t$  is a step-dependent weighting term balancing noise levels across timesteps. For the generation, the denoised latent representation is decoded through the VAE decoder for the RGB image output.

## C. Extended Implementation Details

### C.1. VQ-VAE Specifications

Our baseline VLM, Janus-Pro 7B, employs a VQ-GAN-style VQ-VAE as its image tokenizer for visual generation. The tokenizer encodes each RGB image into an 8-channel latent representation with a  $16 \times$  spatial downsampling factor, producing a  $24 \times 24$  grid (576 locations) for a  $384 \times 384$  input resolution. In a standard VQ-VAE pipeline, each latent vector at every spatial location is vector-quantized by selecting the nearest entry from a codebook of 16,384 learned embeddings, where each code vector is 8-dimensional; this nearest-neighbor assignment converts the continuous latent representation into a discrete index, forming the discrete visual token sequence used by the autoregressive generator. During VLM-based image generation, the multimodal transformer autoregressively predicts 576 discrete token IDs, each corresponding to one of the 16,384 codebook entries; the selected code vectors are then arranged into an 8-channel  $24 \times 24$  latent grid, which the VQ-VAE decoder maps back to the RGB image space through the learned dequantization and upsampling layers.

In contrast, our **Logit-to-Code Distributional Mapping** does not collapse each latent location to a single nearest-neighbor code. Instead, before the vector-quantization step is applied, we obtain the pre-quantized **Image-Token Features** and

compute their similarity to all 16,384 codebook vectors to obtain a logit distribution over the entire codebook. Rather than selecting a single discrete index, we interpret this distribution as a continuous approximation of the quantization step and obtain a continuous code embedding by computing the probability-weighted sum of all codebook vectors. Consequently, our diffusion-based decoder conditions on continuous code vectors rather than hard codebook assignments, enabling it to preserve fine-grained information that would otherwise be lost due to discrete quantization.

## D. Additional Ablation Studies

### D.1. Effect of Denoising Steps

We study the impact of the diffusion denoising steps on the resulting sample quality. To examine this effect, we evaluate our diffusion-based decoder under different numbers of denoising steps while keeping all other components fixed.

We measure reconstruction performance on the first 1,000 validation images of ImageNet-1K and compare our diffusion outputs to the baseline VQ-VAE decoder of Janus-Pro 7B. Table 6 summarizes the quantitative results.

Table 6. Reconstruction performance of our diffusion-based decoder across different numbers of denoising steps, compared against the Janus-Pro 7B VQ-VAE baseline. The best results are highlighted.

<i>ImageNet-1K Val.</i>	rFID↓	SSIM↑	LPIPS↓
VQ-VAE Decoder	23.1038	0.5756	0.1551
Ours (5 steps)	35.0169	0.5855	0.1918
Ours (10 steps)	20.8859	0.5995	0.1478
Ours (15 steps)	18.3279	<b>0.6012</b>	0.1417
Ours (20 steps)	17.6918	0.5993	0.1405
Ours (25 steps)	<b>17.5659</b>	0.5975	<b>0.1404</b>
Ours (30 steps)	17.6969	0.5954	0.1410
Ours (35 steps)	17.7818	0.5940	0.1414

We observe that even with only 10 denoising steps, our method surpasses the VQ-VAE baseline across all metrics. As the step count increases, rFID and LPIPS continue to improve and reach their best values at 25 steps, after which the performance gradually degrades. SSIM, on the other hand, peaks earlier at 15 steps, suggesting that global structure is recovered in the initial stages of denoising, while subsequent steps mainly refine texture and low-frequency details. Together, these observations indicate that the diffusion trajectory rapidly establishes the core scene layout, with additional steps primarily polish perceptual details rather than altering structural content.

## E. Additional Results on Multiple VLMs

### E.1. Image Reconstruction

We additionally evaluate our method on a different VLM backbone, LlamaGen-XL, operating at a spatial resolution of  $256 \times 256$ . Quantitative and qualitative results are presented in Figure 10 and Table 7. Because LlamaGen-XL employs the same  $16 \times$  spatial downsampling factor as Janus-Pro 7B, its lower input resolution provides substantially fewer spatial samples for the diffusion decoder, making the reconstruction task considerably more challenging than in the  $384 \times 384$  Janus-Pro setting. Despite this reduced information, our method achieves superior rFID performance and competitive scores on SSIM and LPIPS compared to baseline VQ-VAE, demonstrating that the proposed diffusion-based decoder remains effective in image reconstruction even under complicated low-resolution conditions.

Table 7. Quantitative image reconstruction results ( $256 \times 256$  resolution) using LlamaGen-XL. We evaluate image reconstruction on ImageNet-1K and MJHQ-30K, reporting metrics averaged across all classes and categories. It compares the LlamaGen-XL baseline’s native VQ-VAE decoder and our diffusion-based decoder. Superior results are highlighted.

<i>ImageNet-1K Val.</i>	rFID↓	SSIM↑	LPIPS↓
VQ-VAE Decoder	4.1919	0.5566	<b>0.1388</b>
<i>LCDM+LC+DCDD</i> (ours)	<b>1.4087</b>	<b>0.5600</b>	0.1404
<i>MJHQ-30K</i>	rFID↓	SSIM↑	LPIPS↓
VQ-VAE Decoder	4.9653	<b>0.6140</b>	<b>0.1407</b>
<i>LCDM+LC+DCDD</i> (ours)	<b>1.9028</b>	0.6060	0.1484

### E.2. Text-to-Image Generation

We present additional text-to-image generation results comparing the Janus-Pro 7B baseline (VQ-VAE decoding) with our diffusion-based decoder in Figure 9.

We also evaluate our method on LlamaGen-XL for the text-to-image generation task. Quantitative and qualitative comparisons are presented in Figure 11 and Table 8. In contrast to the substantial improvements observed with Janus-Pro 7B, our method yields only marginal gains on LlamaGen-XL, showing slight improvements in Single-Object and Counting accuracy on GenEval, while the remaining categories exhibit comparable or mildly degraded performance.

This trend appears to stem from the weak baseline performance of the LlamaGen-XL backbone. The baseline VQ-VAE decoding displays very low image fidelity and weak text-image alignment (e.g., only 30% GenEval overall accuracy and high gFID on MJHQ-30K), indicating that the underlying image-token sequences produced by the model already contain substantial semantic and perceptual errors. Because our diffusion-based decoder is designed to enhance

Table 8. Quantitative text-to-image generation results (256×256 resolution) using LlamaGen-XL. We evaluate MJHQ-30K and GenEval metrics, respectively: MJHQ measures generation FID (lower is better), while GenEval assesses semantic correctness across object existence, attributes, counting, and spatial relations (higher is better). Superior results are highlighted.

<b>MJHQ-30K</b>											
	Overall	Animals	Art	Fashion	Food	Indoor	Landscape	Logo	People	Plants	Vehicles
VQ-VAE Decoder	59.0292	74.1959	82.9698	92.8457	86.4562	89.2189	82.0326	68.5263	105.9981	87.2854	82.0326
<b>LCDM+LC+DCDD (ours)</b>	61.0925	74.6621	87.1321	104.2776	93.6168	96.6309	90.0496	<b>66.9729</b>	114.4049	93.7683	90.0496

<b>GenEval</b>		Overall	Single	Two	Counting	Colors	Position	Color Attr.
VQ-VAE Decoder		30.02	69.06	32.32	14.69	55.85	5.25	3.00
<b>LCDM+LC+DCDD (ours)</b>		28.19	70.94	25.76	19.38	47.07	4.25	1.75

the fidelity of the VLM’s intended outputs rather than alter their semantics, it heavily depends on the quality of the token sequence provided by the VLM.

When the conditioning tokens themselves are severely flawed, the decoder receives an input signal that lacks coherent semantic structure. In such cases, the additional expressive capacity of our diffusion model cannot compensate for the deficiencies of the backbone VLM; instead, the diffusion process may magnify the underlying errors, leading to further degradation.

**F. Limitation**

A primary strength of our method is its ability to enhance the visual fidelity of images decoded from VLM-generated image tokens while preserving the visual intent of the underlying VLM. This fidelity enhancement is also reflected in quantitative evaluations such as GenEval, where our decoder achieves higher text–image alignment scores. However, despite these improvements, our approach remains fundamentally limited by the semantics encoded in the VLM’s predicted token sequence. Because the decoder operates strictly on the image tokens provided by the VLM, it is unable to rectify conceptual or high-level semantic errors present in those tokens.

As illustrated in Figure 7, the model can sharpen the shapes of the letters in a “STOP” sign, yet it cannot correct the misspelling “STOPP;” which originates from the VLM’s token generation. Similarly, it cannot correct the implausible or anatomically inconsistent structure of the distorted cow. Our method specifically addresses the fidelity limitations imposed by discrete token decoders and is not designed to modify or reinterpret the semantic content produced by the VLM.

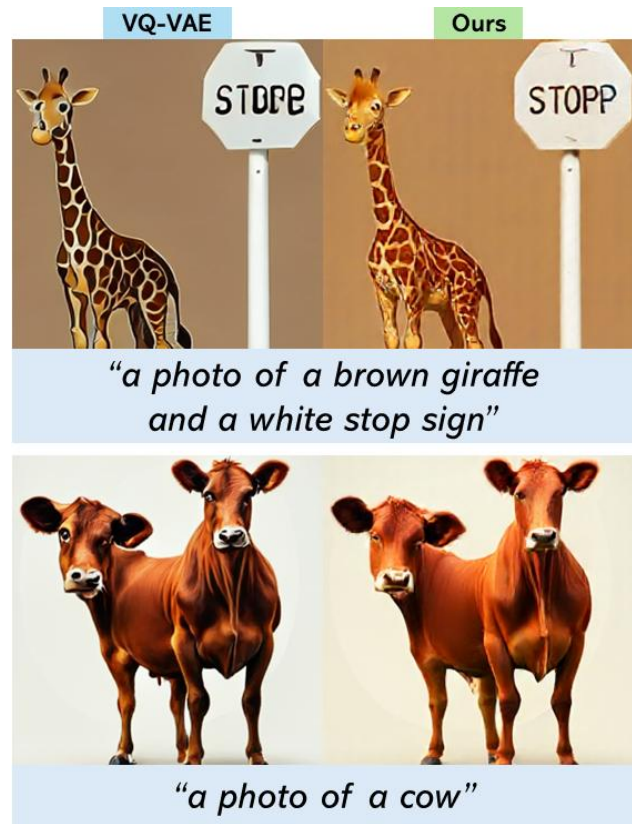


Figure 7. Illustrations of the limitation of our method in the Text-to-Image generation. While our diffusion-based decoder enhances visual fidelity compared to the VQ-VAE decoder of Janus-Pro 7B, it cannot correct semantic errors generated by the VLM.



Figure 8. Additional qualitative image reconstruction results ( $384 \times 384$  resolution) using Janus-Pro-7B. We compare the baseline VQ-VAE decoder with our diffusion-based decoder. The top two rows show samples from ImageNet-1K, and the bottom two rows show samples from MJHQ-30K.

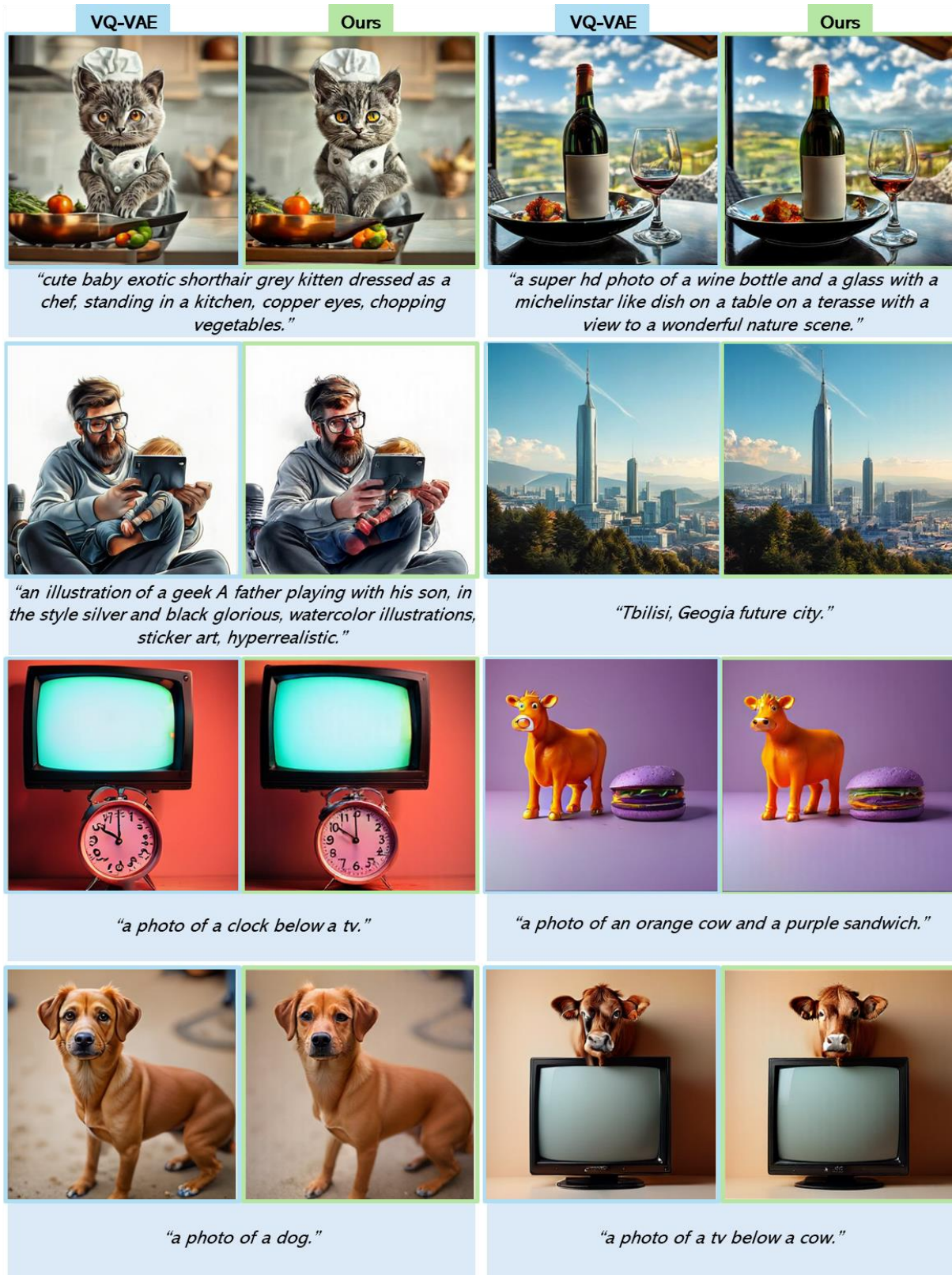


Figure 9. Additional qualitative text-to-image samples ( $384 \times 384$  resolution) generated using Janus-Pro-7B. We compare the baseline VQ-VAE decoder with our diffusion-based decoder. Prompts in the upper two rows are drawn from MJHQ-30K, and those in the lower two rows from GenEval.

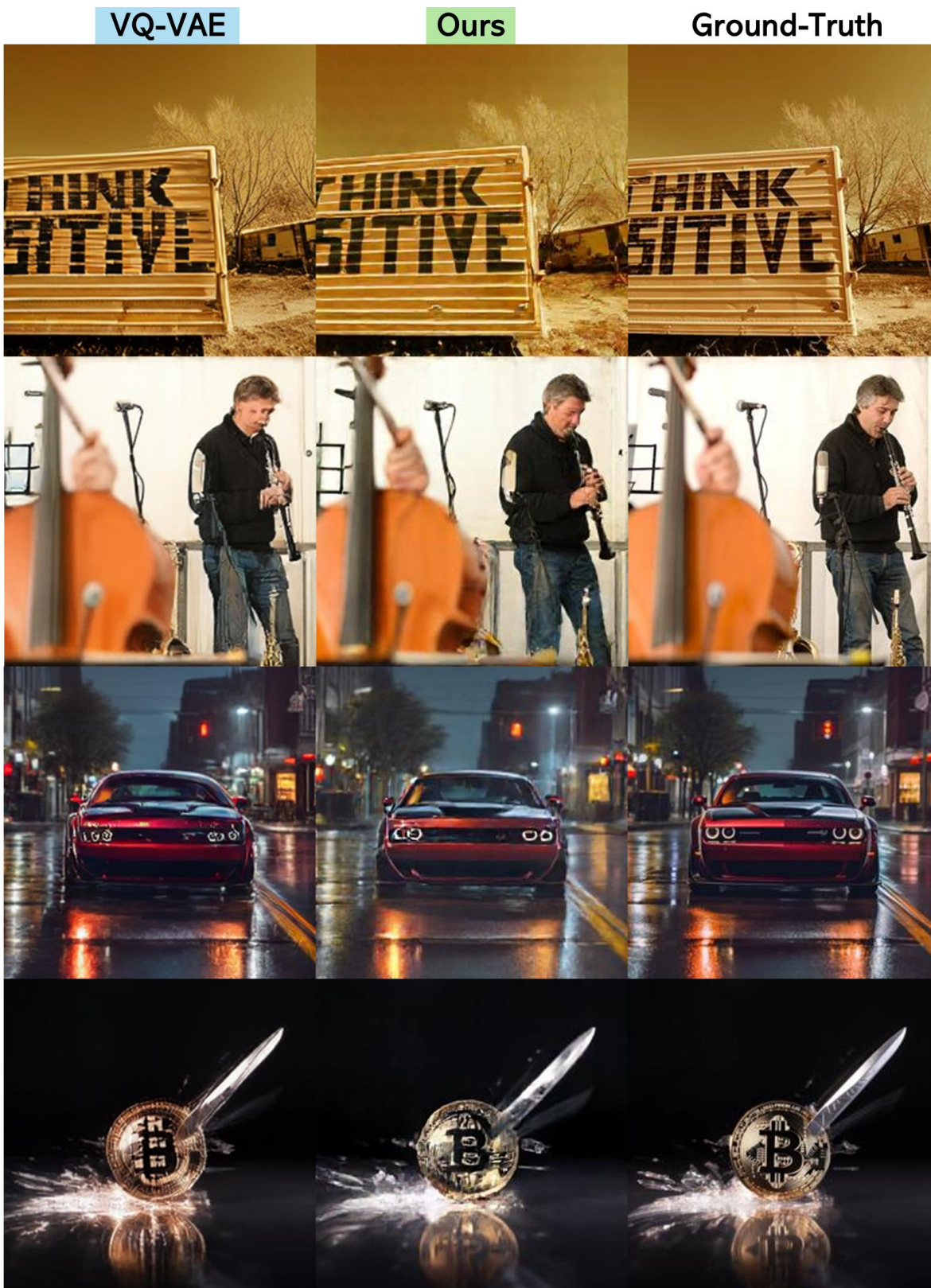


Figure 10. Qualitative image reconstruction results ( $256 \times 256$  resolution) using LlamaGen-XL. We compare the baseline VQ-VAE decoder with our diffusion-based decoder. The top two rows show samples from ImageNet-1K, and the bottom two rows show samples from MJHQ-30K.

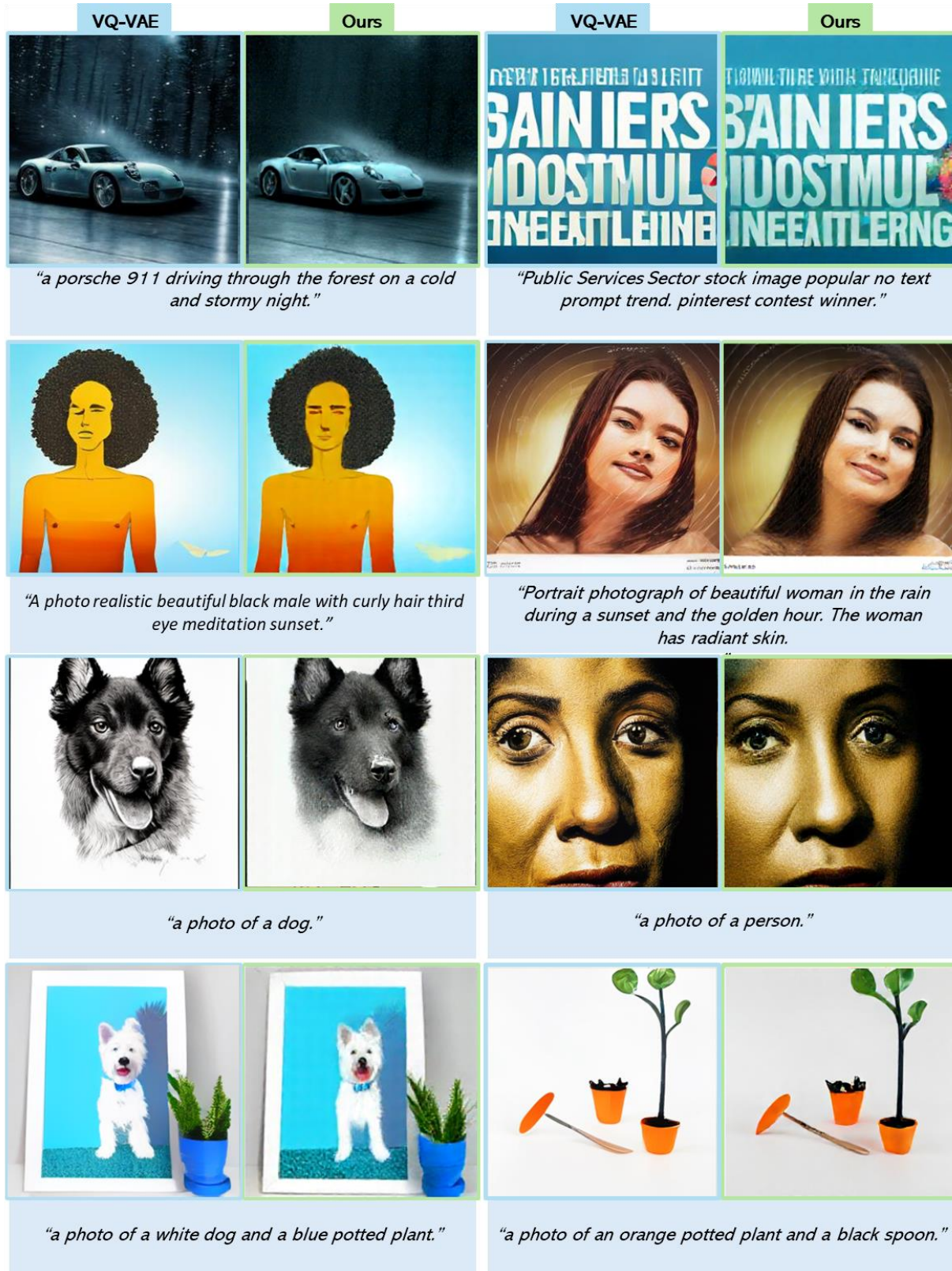


Figure 11. Qualitative text-to-image results (256×256 resolution) using LlamaGen-XL. We compare the baseline VQ-VAE decoder with our diffusion-based decoder. Prompts in the upper two rows are drawn from MJHQ-30K, and those in the lower two rows from GenEval.